

Dynamics and Resilience of the Charge Density Wave in a Bilayer Kagome Metal

Manuel Tuniz**,¹ Armando Consiglio**,² Denny Puntel,¹ Chiara Bigi,³ Stefan Enzner,² Ganesh Pokharel,⁴ Pasquale Orgiani,⁵ Wibke Bronsch,⁶ Fulvio Parmigiani,^{1,6} Vincent Polewczyk,⁵ Phil D. C. King,³ Justin W. Wells,⁷ Ilija Zeljkovic,⁸ Pietro Carrara,^{9,5} Giorgio Rossi,^{9,5} Jun Fujii,⁵ Ivana Vobornik,⁵ Stephen D. Wilson,⁴ Ronny Thomale,² Tim Wehling,^{10,11} Giorgio Sangiovanni,² Giancarlo Panaccione,⁵ Federico Cilento,^{6,*} Domenico Di Sante,^{12,13,†} and Federico Mazzola^{14,5,‡}

¹*Dipartimento di Fisica, Universita degli studi di Trieste, 34127, Trieste, Italy*

²*Institut für Theoretische Physik und Astrophysik and
Würzburg-Dresden Cluster of Excellence ct.qmat,
Universität Würzburg, 97074 Würzburg, Germany*

³*School of Physics and Astronomy, University of St Andrews,
St Andrews KY16 9SS, United Kingdom*

⁴*Materials Department, University of California Santa Barbara,
Santa Barbara, California 93106, USA*

⁵*Istituto Officina dei Materiali, Consiglio Nazionale delle Ricerche, Trieste I-34149, Italy*

⁶*Elettra - Sincrotrone Trieste S.C.p.A.,
Strada Statale 14, km 163.5, Trieste, Italy*

⁷*Centre for Materials Science and Nanotechnology,
University of Oslo (UiO), Oslo 0318, Norway.*

⁸*Department of Physics, Boston College, Chestnut Hill, MA 02467, USA*

⁹*Dipartimento di Fisica, Università degli Studi di Milano, via Celoria 16, 20133 Milano, Italy*

¹⁰*Institute of Theoretical Physics, University of Hamburg,
Notkestrasse 9, 22607 Hamburg, Germany*

¹¹*The Hamburg Centre for Ultrafast Imaging,
Luruper Chaussee 149, 22761, Hamburg, Germany*

¹²*Department of Physics and Astronomy,
University of Bologna, 40127 Bologna, Italy*

¹³*Center for Computational Quantum Physics,*

Flatiron Institute, 162 5th Avenue, New York, NY 10010, USA

¹⁴*Department of Molecular Sciences and Nanosystems,
Ca' Foscari University of Venice, 30172 Venice, Italy*

(Dated: February 22, 2023)

Abstract

Long-range electronic order descending from a metallic parent state constitutes a rich playground to study the intricate interplay of structural and electronic degrees of freedom¹⁻⁵. With dispersive and correlation features as multifold as topological Dirac-like itinerant states, van-Hove singularities, correlated flat bands, and magnetic transitions at low temperature, kagome metals are located in the most interesting regime where both phonon and electronically mediated couplings are significant⁶⁻¹¹. Several of these systems undergo a charge density wave (CDW) transition, and the van-Hove singularities, which are intrinsic to the kagome tiling, have been conjectured to play a key role in mediating such an instability. However, to date, the origin and the main driving force behind this charge order is elusive. Here, we use the topological bilayer kagome metal ScV_6Sn_6 as a platform to investigate this puzzling problem, since it features both kagome-derived nested Fermi surface and van-Hove singularities near the Fermi level, and a CDW phase that affects the susceptibility, the neutron scattering, and the specific heat², similarly to the siblings $A\text{V}_3\text{Sb}_5$ ($A = \text{K}, \text{Rb}, \text{Cs}$)^{1,12} and FeGe ¹³. We report on our findings from high—resolution angle-resolved photoemission, density functional theory, and time-resolved optical spectroscopy to unveil the dynamics of its CDW phase. We identify the structural degrees of freedom to play a fundamental role in the stabilization of charge order. Along with a comprehensive analysis of the subdominant impact from electronic correlations, we find ScV_6Sn_6 to feature an instance of charge density wave order that predominantly originates from phonons. As we shed light on the emergent phonon profile in the low-temperature ordered regime, our findings pave the way for a deeper understanding of ordering phenomena in all CDW kagome metals.

** These authors contributed equally

Bilayer kagome metals are an emerging class of correlated topological compounds with chemical formula RV_6Sn_6 (R : rare earth - hereafter also dubbed as the 166 family), featuring unconventional topological phases and collective magnetic excitations at low temperature^{2,10,11,14–18}. Similarly to the sister compounds AV_3Sb_5 (A : alkali atoms - hereafter also nicknamed as the 135 family), the electronic structure of RV_6Sn_6 is a rich platform for the emergence of unconventional phase diagrams, boasting the simultaneous presence of itinerant Dirac electrons, non-trivial flat bands, and van-Hove singularities at the Fermi energy^{1,6–9,19–22}. Among the 166 family, ScV_6Sn_6 exhibits a unique three-dimensional charge density wave (CDW) transition, with a motif dissimilar to those observed in other kagome compounds¹². Here, the CDW phase provokes a weak atomic lattice displacement, which might generate unconventional phenomena, such as metal-insulator transitions of fermions, vortexes at the surface, chiral currents, and bond orders^{2,23–30}. The major goal of contemporary research thus is to reveal the underlying mechanism of the charge order in ScV_6Sn_6 and the specific role of structural and electronic degrees of freedom, the interdependence of whom has so far remained uncharted territory.

Previous works have highlighted important differences between the CDW in ScV_6Sn_6 , AV_3Sb_5 , and $FeGe$ ¹³. In AV_3Sb_5 , the charge order has been thought to be connected to the nesting of the Fermi surface, exemplified by the van-Hove singularity electron filling^{12,31–33}. In these systems, the charge order has been conjectured to be linked to the emergence of superconductivity and stripe orders^{30,34–39}. In addition, the atomic displacement following the onset of the CDW involves mostly the V atoms and their in-plane positions. ScV_6Sn_6 , surprisingly, does not undergo any superconducting transition at low temperature and the motif of the CDW, generated by the ordering vector $Q = (1/3, 1/3, 1/3)$, does not give rise to either the Star of David or trihexagonal arrangement, as for the AV_3Sb_5 compounds, for which the ordering vectors are $Q = (1/2, 1/2, 1/4)$ and $Q = (1/2, 1/2, 1/2)$ ^{33,40,41}. This is ascribed to the involvement of Sn and Sc atoms in the lattice modulation. The differences between these two systems, are also reflected in a much more rapid CDW suppression for ScV_6Sn_6 under the application of pressures⁴², offering an increased ease of tuneability compared to AV_3Sb_5 .

In CDW materials, the simultaneous occurrence of a lattice displacement and a change in the electronic structure, often associated with the opening of gaps in the electronic spectrum challenges the understanding of the main driving force behind the charge order and limits the access to possible consequent or concomitant cascade of collective phases and their control. While there

is compelling evidence of CDW in kagome systems, its microscopic origin and dynamics are still debated. We stress that the understanding of such origin and dynamics is a task of paramount importance given the peculiar electronic structure of kagome with van-Hove singularities at the Fermi level and the presence of a nested Fermi surface, which hints at an energy gain upon a gap opening as an underlying driver. For 166, which has also a topological nature, it becomes crucial to understand the dynamics of the CDW, to uncover not only the relationship between subsequent ordered phases, but to elucidate the interplay between phase transition and electron spins^{11,33,43–46}. In the present study, we used time-resolved optical spectroscopy (TR-OS) to unveil the dynamics of the CDW in the 166 bilayer kagome ScV_6Sn_6 . Specifically, by using TR-OS, we disclose the energy scales involved in the charge order, which points towards a major robustness of the lattice degree of freedom for the observed transition.

First, we describe the electronic properties of ScV_6Sn_6 , then we will show by using ARPES, DFT, and TR-OS how the electronic and structural degrees of freedom are affected by the CDW order. Along with the crystal structure (both with and without CDW) and the Brillouin zone (Figs. 1 **a-b**), we show the expected electronic structure from density functional theory (DFT), above and below the transition temperature, in Fig. 1 **c** (red color without CDW, green shades with CDW). In both CDW and pristine cases, the Dirac-like states and the van-Hove singularities are similar and identifiable, with negligible variation in their electronic dispersion along the Γ -K-M- Γ path. According to the calculations, the van-Hove singularities are located around the Fermi level. It is thus noteworthy that large changes at E_F are not seen upon inclusion of the CDW nested systems^{47–50}. Along the Γ -K-M- Γ high-symmetry direction, the main changes occur at the Γ point within the energy window $[-0.75, -1]$ eV. Below the transition temperature, the separations between the bands increase by approximately 30 meV compared to the electronic structure without CDW (see red box in Fig. 1 **c**). Other changes along the same direction, even if smaller, are indicated by the blue arrows (labeled as '2'). If in the plane that comprises the Γ point, the changes are rather subtle, our DFT calculation reveals that the CDW has its major effect along the A-H and A-L directions (see yellow arrows labeled as '3'). There, we notice that the charge order opens several energy gaps along the entire k -space path. Nonetheless, we also notice that the spectral weight immediately fades away from the gap openings. In addition, the spectral intensity in the CDW phase is still located around the poles of the electronic structure of the bands above T_{CDW} . As a result, the gaps themselves are expected to be challenging to detect experimentally given the vicinity to the poles, the k_z broadening, and the experimental resolution (~ 15 meV, that is larger than the gap value

itself)⁵¹.

Similarly to other 166 materials, as shown in Fig. 2, ScV_6Sn_6 shows the presence of surface states, after the ultrahigh vacuum (UHV) cleave (see Methods for details about the samples' preparation). These surface states have been extensively discussed for other kagome systems^{6,7,32} and members of the 166 family^{10,11,14–16}. While they offer an interesting platform for exploiting spin-momentum locking because of their non-trivial topology^{11,52–55}, they could challenge the clear visualization of small changes occurring in the bulk electronic structure as a consequence of the charge order, because they could obfuscate subtle spectroscopic features. Thus, to exclude this avenue, we measured the electronic structure above and below the transition temperature T_{CDW} and along the Γ -K-M- Γ high symmetry direction, with and without surface states such that one can better distinguish the bulk from the surface-derived signal (see Fig.2 for the clean surface case with both light polarizations and Supplementary Information Figs. 1 and 2 for data where the surface states have been suppressed and how). Along the selected high-symmetry path, we have the most favorable photoemission matrix elements and the intensity of the bands is the most prominent. Notably, no remarkable differences are observed across T_{CDW} , besides a constant thermal broadening which affects the spectra collected above T_{CDW} .

To still check possible effects of the charge order, from the ARPES spectra collected along the Γ -K-M- Γ path, we extracted energy-distribution curves (EDCs) across the Γ point, where we expect the strongest changes induced by the CDW (Fig.2 i-I and red box of Fig.1 c). By using linear-horizontal (LH) polarized light, it is hardly possible to see the relevant states affected by the charge order (see Fig.2 i). By using linear-vertical (LV), instead, the missing spectral weight is recovered. In this condition, we resolve a 70 meV splitting at approximately 0.8 eV of binding energy. Such a splitting might be consistent with the calculated increase in the energy separation produced by the CDW, however, we cannot exclude that this might be an effect of the band sharpening due to the lower temperature (see Fig.2 I). Despite having weaker intensity due to photoemission matrix elements, we also collected ARPES spectra along the A-L and A-H high-symmetry directions (shown in Supplementary Information Figs. 3, 4, and 5). Along these paths, the DFT analysis predicts the strongest changes in the electronic structure. Unfortunately, the changes from above to below T_{CDW} are very small and not well-resolved experimentally. This is likely due, as anticipated above, to the combination of k_z broadening, finite experimental resolutions, small energy values of the gaps, and expected spectral weight concentrated along the poles of the bands above the CDW transition.

The ARPES data depict a situation where most of the electronic spectral weight is only weakly affected by the CDW order in the proximity of the Fermi level (within the experimental resolutions). This is in line with DFT only showing a partial gap opening, which involves only certain bands but not the majority of the V-derived spectral weight. In addition, the partial gap calculated in the electronic structure agrees well with recent optical measurements in the static regime performed for ScV_6Sn_6 , which show a sharp first order transition without the development of full gaps in the optical spectra². Importantly, this behaviour describes a rather rare phenomenology, which is different from the most commonly observed second-order density condensation gaps, found in systems which undergo a CDW transition. In other words, the inability to spectroscopically resolve changes in the Fermi surfaces across the transition temperature makes ScV_6Sn_6 reminiscent of the CDW behaviour discovered for IrTe_2 , TaTe_2 , and BaNi_2As_2 ^{11,56,57}. This aspect is intimately related to the underlying electronic structure of the compound; the vanadium states indeed contribute in a significant way to the density of states around E_F , while the corresponding atoms are not influenced by the CDW displacement. Conversely, tin and scandium states are not predominant at E_F while the corresponding atoms' positions are particularly influenced by the CDW transition. Additionally, ScV_6Sn_6 shows a very peculiar ordered phase, with a marked peak in the specific heat and an increased metallic character below the transition². However, the origin of the charge order is still an open question. It is then crucial to separate the time- and energy-scales of the electronic and lattice degrees of freedom and to determine their robustness and involvement in the CDW order.

To this aim, we use TR-OS and we measure the time-resolved reflectivity dynamics of ScV_6Sn_6 . Fig.3 a presents the temperature (T) dependence of the photoinduced reflectivity transients, $\Delta R/R$, recorded upon increasing the temperature (T from approximately 18 K; the fluence was $F \approx 0.2 \text{ mJ/cm}^2$). The $\Delta R/R$ can be described by two features: an incoherent (non-oscillating) response and a coherent oscillatory behaviour. In our data, clear oscillations in the $\Delta R/R$, showing a strong T-dependence, are detected up to the transition temperature T_{CDW} (Fig.3 a-b). The incoherent (non-oscillating) response consists of two decays, a fast and a slow one, with characteristic times τ_1 and τ_2 , respectively (see Supplementary Information for details about the data analysis and their extraction) that appear in the data as a fast peak and a slowly-decaying component. Similarly to the coherent response, the incoherent one is also strongly T-dependent and it shows the indication of a phase transition around $T \approx 90 \text{ K}$ (see Fig.4 a), which matches well with the nominal T_{CDW} ². Above T_{CDW} , the $\Delta R/R$ becomes smaller and, after the fast exponential decay,

it changes sign becoming negative (see trace '5' of Fig.3 b).

In general, below the critical CDW temperature, the pump pulse induces an abrupt change in the reflectivity, followed by a fast decay within a picosecond and a slower recovery on a timescale of the order ≈ 10 ps^{58–62}. The first, which slows down critically upon approaching the transition temperature, is attributed to the re-opening of the CDW gap, while the second one, as confirmed by detailed studies of the dynamics as a function of the excitation fluence and applied external electric field, is attributed to a second stage of the CDW recovery^{63–66}. In ScV₆Sn₆, the T-evolution of the incoherent part of the $\Delta R/R$ shows a rather peculiar behavior: in contrast to the well-studied one dimensional CDW systems, the lifetime of the first fast decay τ_1 increases linearly with the temperature and shows a rapid drop at T_{CDW} (Fig.4 a). Remarkably, no divergence of the lifetime τ_1 is observed during the phase transition. This peculiar behavior, in combination with our ARPES measurements and DFT analysis, suggests an unusual origin for the CDW phase in this material, where no gaps are observed in the near Fermi level region. Indeed, a divergence of the lifetime τ_1 is usually linked to the closing of the electronic gap that develops in conventional CDW transitions. This is also different from what has been observed in the kagome metal CsV₃Sb₅, where TR-OS measurements have highlighted the divergence of the lifetime of the fast decay process during the onset of the charge order³⁸.

Interestingly, from the fits to the data (see Supplementary Information for more details), the frequency of the oscillatory mode and the damping show a pronounced temperature dependence, as we show in Fig.4 b. In particular, at low temperature the mode is characterized by a frequency of ~ 1.45 THz, in excellent agreement with our ab-initio estimate of 1.42 THz from the quadratic fit of the DFT total energy around the minimum of CDW ordered structure (see Fig.4 c and Methods for more details), and we observe a ≈ 6 % softening of the mode frequency and an exponential increase of the damping constant, when the temperature of the system approaches the critical temperature of the CDW transition. Such a temperature dependence has been observed in many CDW systems and it constitutes the fingerprint of an amplitude mode (AM) of the CDW phase^{61,62,67–70}. This observation confirms that the coherent response is not due to a trivial phonon, but rather to the excitation of the AM of the CDW phase, confirming the onset of CDW physics in ScV₆Sn₆. We also note that no fingerprints of an AM have been hitherto detected in CsV₃Sb₅ by previous reflectivity studies³⁸.

By varying the excitation density (fluence), additional information about the nature of the phase transition can be obtained. The melting of electronic modulation is generally achieved on a

timescale much faster than the characteristic timescale related to the relaxation of the periodic lattice modulation, which is given by the period of the characteristic amplitude modes of the system. This results in the disentanglement of electronic and lattice degrees of freedom on the sub-picosecond time scale, with a subsequent rapid recovery of the electronic degrees of freedom^{61,69,71,72}. Additionally, the characteristic energy required to fully drive the phase transition, i.e. quenching the periodic lattice distortion and the electronic degrees of freedom, is that one which leads to the disappearance of the (oscillatory) amplitude mode^{60,71}. This provides a means to quantify the strength of the lattice degree of freedom compared to the electronic one. We report this in Fig. 3 c, where the evolution of the scaled $\Delta R/R$ signal as a function of the fluence is shown, in a range from ~ 50 to $\sim 1000 \mu\text{J}/\text{cm}^2$. The traces are scaled to the fluence to better visualize the qualitative behavior of the response upon approaching the photoinduced phase transition. Note that the sample is kept at a temperature well-below T_{CDW} . In the low perturbation regime, the signal scales linearly with excitation density (traces A, B, C in Fig. 3 d), while upon approaching the photoinduced phase transition the $\Delta R/R$ signal related to CDW order shows saturation^{60,71}. The maximum change that can be induced in the signal is generally achieved when the electronic degree of freedom associated to the CDW order is collapsed. We find that the fast electronic component with relaxation time τ_1 saturates at a fluence, where the oscillations linked to AM involving the lattice degrees of freedom persist^{58,71,73}. By progressively increasing the excitation fluence, the oscillations in the $\Delta R/R$ due to the AM get also suppressed, with an exponential increase of the damping constant and a softening of the frequency of the mode. Remarkably, our measurements highlight the robustness of the lattice reconstruction of the CDW in this material. Indeed, even at high excitation fluences ($\sim 700 \mu\text{J}/\text{cm}^2$), the oscillations due to the AM are still detected. This behavior is again markedly different from what has been observed in the sister compound CsV_3Sb_5 , where already at a pump fluence as small as $\sim 55 \mu\text{J}/\text{cm}^2$, the CDW order is melted³. In our study, we show that the oscillation disappears completely only at a fluence of $\sim 1000 \mu\text{J}/\text{cm}^2$, meaning that the lattice order can be melted, although at a fluence larger than the one required to saturate the purely electronic response at around $\approx 240 \mu\text{J}/\text{cm}^2$. The electronic states that maximally couple to this CDW span an energy window around the Fermi level of about 0.25 eV, because smearing over that window greatly affects the AM, as we show in Fig. 4 d. Indeed, taking into account the electronic specific heat of ScV_6Sn_6 , an absorbed fluence of $\approx 240 \mu\text{J}/\text{cm}^2$ leads to an increase of the electronic temperature of ≈ 2100 K, which is in reasonable agreement with the smearing obtained by DFT calculations (See Fig. 4 d). Finally, it

is only when the average lattice temperature exceeds the CDW critical temperature because of the average power deposited by the pump pulse, that one might expect to detect the transient signal of the high-temperature phase. We estimate the pump-induced average heating to be in a $\Delta T \approx 20$ K at a fluence of ≈ 1 mJ/cm². Hence, in order to reach T_{CDW} , very large fluences are required, which are not attainable because sample damage would occur.

In conclusion, by using the combination of experimental techniques, i.e. ARPES and TR-OS, as well as theoretical calculations, we disclose the dynamics of the unusual CDW transition in ScV₆Sn₆ and we simultaneously demonstrate marginal energy gaps at the Fermi level. In particular, temperature dependent TR-OS reveals the hallmarks of the CDW. In addition, our fluence dependent study disentangles the electronic and structural degrees of freedom, showing persisting AM oscillation up to unusually high values of fluence, corroborating the robustness of the lattice distortions compared to the sudden disruption of the purely electronic component. Such dynamics is in favor of a CDW with the lattice degrees of freedom and electron-phonon interaction playing the dominant role. We believe that our comprehensive study sheds light onto the collective modes emerging in the low-temperature phase of ScV₆Sn₆. It paves the way for the understanding of unconventional many-body phases in correlated kagome metals, which all share a similarly nested Fermi surface, and deepens our understanding of cooperative lattice and electronic symmetry breaking at this new frontier. Therefore, we think that our discovery is the crucial step to understand the origin and drive of the CDW also in the archetypal family AV₃Sb₅.

Methods

Experimental details – Single crystals of ScV₆Sn₆ were grown using a flux-based growth technique as reported in the reference⁷⁴. Sc (chunk, 99.9%), V (pieces, 99.7%), and Sn (shot, 99.99%) were loaded inside an alumina crucible with the molar ratio of 1:6:20 and then heated at 1125 °C for 12 h. Then, the mixture was slowly cooled to 780 °C at a rate of 2 °C/h. Thin plate-like single crystals were separated from the excess Sn-flux via centrifuging at 780 °C. The samples were cleaved in ultrahigh vacuum (UHV) at the pressure of 1×10^{-10} mbar. The ARPES data were acquired at the APE-LE end station (Trieste) using a VLEED-DA30 hemispherical analyzer. The energy and momentum resolutions were better than 12 meV and 0.02 \AA^{-1} , respectively. The temperature of the measurements was kept constant throughout the data acquisitions (16 K and 120 K, below and above T_{CDW} respectively). Both linear polarizations were used to collect the data from the APE undulator of the synchrotron radiation source ELETTRA (Trieste). The photon energy used for the ARPES data was 75 eV. This choice was such that the spectra intensity was the

most prominent, especially near the region of the quadratic minimum of the electronic structure, where the major changes with the CDW are expected.

Time-resolved reflectivity experiments were performed at the T-ReX laboratory (FERMI, in Trieste) with a probe photon energy of ≈ 0.95 eV (1300 nm). The measurements were performed using a Ti:sapphire femtosecond (fs) laser system, delivering, at a repetition rate of 250 kHz, ≈ 50 fs light pulses at a wavelength of 800 nm (1.55 eV). The single color probe measurements were performed at a probe wavelength of 1300 nm, obtained by filtering a broadband (0.8–2.3 eV) supercontinuum probe beam, generated using a sapphire window.

Theoretical details – DFT calculations have been performed using both Quantum Espresso and VASP packages. Phonon calculations are based on density functional perturbation theory, as implemented in Quantum Espresso^{75–77}. Exchange and correlation effects were included with the generalized gradient approximation (GGA) using the Perdew-Burke-Ernzerhof (PBE) functional⁷⁸; the pseudopotentials are norm-conserving and scalar relativistic, containing core corrections⁷⁹. Self-consistent calculations and ionic relaxation of the unit cell have been performed with a $9 \times 9 \times 6$ k -grid; convergence threshold for both ionic minimization and electronic self-consistency are set to be 10^{-15} Ry. The kinetic energy cutoff for the wavefunctions is equal to 90 Ry. A ordinary Gaussian spreading of 0.006 Ry has been used. Once the structure was properly at equilibrium, with vanishing forces acting on each atom, we proceeded with the actual phonon calculations. The dynamical matrices have been obtained and computed for a q -grid of $3 \times 3 \times 6$, with a self-consistency threshold of 10^{-15} Ry. These dynamical matrices are consequently Fourier-transformed to obtain the inter-atomic force constants (IFC) in real space; three translational acoustic sum rules have been imposed, via correction of the IFC. Finally, both phonon dispersion and phonon density of states are obtained. In particular, for the density of states calculations (see results in the Supplementary Information) we used $30 \times 30 \times 30$ q -points. The presence of imaginary phonon modes has been verified also for a $6 \times 6 \times 9$ and a $9 \times 9 \times 12$ q -grid, during the dynamical matrices' calculation. The remaining DFT calculations have been performed with VASP. To study the dependence of the CDW phase with respect to the smearing we used a plane-wave cutoff of 500 eV and a $9 \times 9 \times 9$ Γ -centered k -mesh. Ionic relaxations have been performed with a constant volume. The relaxations of the ionic and electronic degrees of freedom were considered converged respectively below a threshold of 10^{-5} eV and 10^{-10} eV. Subsequently, for each smearing value, we computed the norm of the 351-dimensional (117 atoms \times 3) displacement vector among the CDW and the pristine phases. Spin-orbit coupling has not been included for this

set of calculations. To study the structural interpolation among the CDW and pristine systems, leading to the double-well potential profile, we computed the 351-dimensional displacement vector \vec{e} between the two configurations. This has a norm of $\sim 0.64 \text{ \AA}$. The two structures hence are gradually interpolated, moving the atoms along the direction defined by \vec{e} . For each step, a self-consistent calculation with 500 eV for the kinetic energy cutoff and a Γ -centered $12 \times 12 \times 12$ k -grid has been performed. The smearing here is constant and equal to 0.005 eV. The electronic calculations are considered converged below a threshold of 10^{-8} eV. This process has been studied while keeping the volume constant. Also here the spin-orbit coupling has not been included. To compute the frequency of the phonon mode we started from a quadratic fit around the minimum of the Born-Oppenheimer potential, corresponding to the CDW phase; the resulting fit has equation $y = 0.379x^2$. From here it is possible to obtain the "spring" constant k , as $k = 2 \times 0.379202 \text{ eV/\AA}^2$. The effective mass m^* is computed using the normalized displacement vector $\hat{n} = \vec{e}/\|\vec{e}\|$ and the mass tensor $\mathbf{M} = \text{diag}(m_1, m_1, m_1, \dots, m_{117}, m_{117}, m_{117})$ via $m^* = \vec{e} \cdot (\mathbf{M} \cdot \vec{e})$; we obtain $m^* = 91.02 \text{ u}$. Note that this mass value is intermediate among the Sn and Sc ones, i.e. the atoms which mostly participate to the CDW transition. Finally the frequency ν can be computed as $\nu = \omega/(2\pi)$, with $\omega = \sqrt{k/m^*}$, giving us $\nu = 1.42 \text{ THz}$. When considering the unfolding of the CDW supercell, the Kohn–Sham wave functions are expanded in plane waves up to a 400 eV energy cutoff, with a k -mesh resolution for the self-consistent electronic structure calculations of 0.02 reciprocal Angstroms. For the non-self-consistent calculations, the k -mesh resolution corresponds to 0.01 reciprocal Angstroms. In this case, the spin-orbit coupling has been considered and included self-consistently. The initial CDW supercell corresponds in every case to the experimental one². Band structures have been visualized using the VASPKIT postprocessing tool⁸⁰. VESTA⁸¹ has been used to visualize the crystal structures.

Acknowledgements The authors acknowledge Andrea Cavalleri for the fruitful discussions on this work. The research leading to these results has received funding from the European Union’s Horizon 2020 research and innovation program under the Marie Skłodowska-Curie Grant Agreement No. 897276. We gratefully acknowledge the Gauss Centre for Supercomputing e.V. (<https://www.gauss-centre.eu>) for funding this project by providing computing time on the GCS Supercomputer SuperMUC-NG at Leibniz Supercomputing Centre (<https://www.lrz.de>). We are grateful for funding support from the Deutsche Forschungsgemeinschaft (DFG, German Research Foundation) under Germany’s Excellence Strategy through the Würzburg-Dresden Cluster of Excellence on Complexity and Topology in Quantum Matter ct.qmat (EXC 2147, Project

ID 390858490) as well as through the Collaborative Research Center SFB 1170 ToCoTronics (Project ID 258499086) and the Hamburg Cluster of Excellence “CUI: Advanced Imaging of Matter” (EXC 2056, Project No. 390715994). This work has been performed in the framework of the Nanoscience Foundry and Fine Analysis (NFFA-MUR Italy Progetti Internazionali) facility. The Flatiron Institute is a division of the Simons Foundation. S.D.W. and G. Po. acknowledge support via the UC Santa Barbara NSF Quantum Foundry funded via the Q-AMASE-i program under award DMR-1906325. F.M. greatly acknowledges the SoE action of pnrr, number SOE.0000068. I.Z. acknowledges the support from U.S. Department of Energy (DOE) Early Career Award DE-SC0020130.

Author contributions F.M., D.D.S and F.C. conceived and designed the project. G.Po. and S.W. grew the crystals. F.M., C.B., J.F., I.V., and P.C. carried out the ARPES measurements, while F.C., M.T., D.P., and W. B. obtained the pump and probe results. A.C. and S.E. performed the numerical calculations and theoretical analysis supervised by D.D.S, G.S., T.W. and R.T. All the authors participated in the discussion and crucially contributed to understanding and the writing of the manuscript.

Additional information Extended data is available for this paper at <https://xxxx>

Supplementary information The online version contains supplementary material available at <https://xxx>

Correspondence and requests for materials should be addressed to Federico Mazzola, Domenico Di Sante and Federico Cilento.

Data availability The data that support the findings of this study are available from the corresponding authors upon reasonable request.

Competing financial interests

The authors declare no competing financial interests.

* federico.cilento@elettra.eu

† domenico.disante@unibo.it

‡ federico.mazzola@unive.it

¹ Neupert, T., Denner, M. M., Yin, J.-X., Thomale, R. & Hasan, M. Z. Charge order and superconductivity in kagome materials. *Nature Physics* **18**, 137–143 (2022). URL <https://www.nature.com/>

- [articles/s41567-021-01404-y](#).
- ² Arachchige, H. W. S. *et al.* Charge density wave in kagome lattice intermetallic ScV₆Sn₆. *Phys. Rev. Lett.* **129**, 216402 (2022). URL <https://link.aps.org/doi/10.1103/PhysRevLett.129.216402>.
 - ³ Wang, Z. X. *et al.* Unconventional charge density wave and photoinduced lattice symmetry change in the kagome metal CsV₃Sb₅ probed by time-resolved spectroscopy. *Phys. Rev. B* **104**, 165110 (2021). URL <https://link.aps.org/doi/10.1103/PhysRevB.104.165110>.
 - ⁴ van Heumen, E. Kagome lattices with chiral charge density. *Nature Materials* **20**, 1308–1309 (2021). URL <https://www.nature.com/articles/s41563-021-01095-z>.
 - ⁵ Luo, H. *et al.* Electronic nature of charge density wave and electron-phonon coupling in kagome superconductor KV₃Sb₅. *Nature Communications* **13**, 273 (2022). URL <https://doi.org/10.1038/s41467-021-27946-6>.
 - ⁶ Kang, M. *et al.* Topological flat bands in frustrated kagome lattice CoSn. *Nature Communications* **11**, 4004 (2020). URL <https://www.nature.com/articles/s41467-020-17465-1>.
 - ⁷ Kang, M. *et al.* Dirac fermions and flat bands in the ideal kagome metal FeSn. *Nature Materials* **19**, 163–169 (2020). URL <https://www.nature.com/articles/s41563-019-0531-0>.
 - ⁸ Lin, Z. *et al.* Flatbands and emergent ferromagnetic ordering in Fe₃Sn₂ kagome lattices. *Phys. Rev. Lett.* **121**, 096401 (2018). URL <https://journals.aps.org/prl/abstract/10.1103/PhysRevLett.121.096401>.
 - ⁹ Ye, L. *et al.* de Haas-van Alphen effect of correlated Dirac states in kagome metal Fe₃Sn₂. *Nature Communications* **10**, 4870 (2019). URL <https://www.nature.com/articles/s41467-019-12822-1>.
 - ¹⁰ Pokharel, G. *et al.* Electronic properties of the topological kagome metals YV₆Sn₆ and GdV₆Sn₆. *Phys. Rev. B* **104**, 235139 (2021). URL <https://journals.aps.org/prb/abstract/10.1103/PhysRevB.104.235139>.
 - ¹¹ Hu, Y. *et al.* Tunable topological Dirac surface states and van Hove singularities in kagome metal GdV₆Sn₆. *Science Advances* **8**, eadd2024 (2022). URL <https://www.science.org/doi/10.1126/sciadv.add2024>.
 - ¹² Kang, M. *et al.* Charge order landscape and competition with superconductivity in kagome metals. *Nature Materials* **22**, 186–193 (2023). URL <https://doi.org/10.1038/s41563-022-01375-2>.

- ¹³ Teng, X. *et al.* Discovery of charge density wave in a kagome lattice antiferromagnet. *Nature* **609**, 490–495 (2022). URL <https://doi.org/10.1038/s41586-022-05034-z>.
- ¹⁴ Peng, S. *et al.* Realizing kagome band structure in two-dimensional kagome surface states of RV_6Sn_6 ($R = \text{Gd, Ho}$). *Phys. Rev. Lett.* **127**, 266401 (2021). URL <https://journals.aps.org/prl/abstract/10.1103/PhysRevLett.127.266401>.
- ¹⁵ Ishikawa, H., Yajima, T., Kawamura, M., Mitamura, H. & Kindo, K. GdV_6Sn_6 : A Multi-carrier Metal with Non-magnetic 3d-electron Kagome Bands and 4f-electron Magnetism. *Journal of the Physical Society of Japan* **90**, 124704 (2021). URL <https://journals.jps.jp/doi/10.7566/JPSJ.90.124704>.
- ¹⁶ Rosenberg, E. *et al.* Uniaxial ferromagnetism in the kagome metal TbV_6Sn_6 . *Phys. Rev. B* **106**, 115139 (2022). URL <https://link.aps.org/doi/10.1103/PhysRevB.106.115139>.
- ¹⁷ Lee, J. & Mun, E. Anisotropic magnetic property of single crystals RV_6Sn_6 ($R = \text{Y, Gd-Tm, Lu}$). *Phys. Rev. Mater.* **6**, 083401 (2022). URL <https://link.aps.org/doi/10.1103/PhysRevMaterials.6.083401>.
- ¹⁸ Chen, D. *et al.* Large anomalous hall effect in the kagome ferromagnet $LiMn_6Sn_6$. *Phys. Rev. B* **103**, 144410 (2021). URL <https://journals.aps.org/prb/abstract/10.1103/PhysRevB.103.144410>.
- ¹⁹ Guo, H.-M. & Franz, M. Topological insulator on the kagome lattice. *Phys. Rev. B* **80**, 113102 (2009). URL <https://journals.aps.org/prb/abstract/10.1103/PhysRevB.80.113102>.
- ²⁰ Mazin, I. I. *et al.* Theoretical prediction of a strongly correlated Dirac metal. *Nature Communications* **5**, 4261 (2014). URL <https://www.nature.com/articles/ncomms5261>.
- ²¹ Kiesel, M. L., Platt, C. & Thomale, R. Unconventional Fermi Surface Instabilities in the Kagome Hubbard Model. *Phys. Rev. Lett.* **110**, 126405 (2013). URL <https://journals.aps.org/prl/abstract/10.1103/PhysRevLett.110.126405>.
- ²² Di Sante, D. *et al.* Turbulent hydrodynamics in strongly correlated Kagome metals. *Nature Communications* **11**, 3997 (2020). URL <https://www.nature.com/articles/s41467-020-17663-x>.
- ²³ Guo, C. *et al.* Switchable chiral transport in charge-ordered kagome metal CsV_3Sb_5 . *Nature* **611**, 461–466 (2022). URL <https://doi.org/10.1038/s41586-022-05127-9>.
- ²⁴ Nishimoto, S., Nakamura, M., O’Brien, A. & Fulde, P. Metal-insulator transition of fermions on a kagome lattice at 1/3 filling. *Phys. Rev. Lett.* **104**, 196401 (2010). URL <https://link.aps.org/>

[doi/10.1103/PhysRevLett.104.196401](https://doi.org/10.1103/PhysRevLett.104.196401).

- ²⁵ Kiesel, M. L., Platt, C. & Thomale, R. Unconventional fermi surface instabilities in the kagome hubbard model. *Phys. Rev. Lett.* **110**, 126405 (2013). URL <https://link.aps.org/doi/10.1103/PhysRevLett.110.126405>.
- ²⁶ Denner, M. M., Thomale, R. & Neupert, T. Analysis of Charge Order in the Kagome Metal AV_3Sb_5 ($A = K, Rb, Cs$). *Phys. Rev. Lett.* **127**, 217601 (2021). URL <https://link.aps.org/doi/10.1103/PhysRevLett.127.217601>.
- ²⁷ Feng, X., Zhang, Y., Jiang, K. & Hu, J. Low-energy effective theory and symmetry classification of flux phases on the kagome lattice. *Phys. Rev. B* **104**, 165136 (2021). URL <https://link.aps.org/doi/10.1103/PhysRevB.104.165136>.
- ²⁸ Park, T., Ye, M. & Balents, L. Electronic instabilities of kagome metals: Saddle points and Landau theory. *Phys. Rev. B* **104**, 035142 (2021). URL <https://link.aps.org/doi/10.1103/PhysRevB.104.035142>.
- ²⁹ Jiang, Y.-X. *et al.* Unconventional chiral charge order in kagome superconductor KV_3Sb_5 . *Nature Materials* **20**, 1353–1357 (2021). URL <https://doi.org/10.1038/s41563-021-01034-y>.
- ³⁰ Liang, Z. *et al.* Three-dimensional charge density wave and surface-dependent vortex-core states in a kagome superconductor CsV_3Sb_5 . *Phys. Rev. X* **11**, 031026 (2021). URL <https://link.aps.org/doi/10.1103/PhysRevX.11.031026>.
- ³¹ Wu, X. *et al.* Nature of Unconventional Pairing in the Kagome Superconductors AV_3Sb_5 ($A = K, Rb, Cs$). *Phys. Rev. Lett.* **127**, 177001 (2021). URL <https://journals.aps.org/prl/abstract/10.1103/PhysRevLett.127.177001>.
- ³² Kang, M. *et al.* Twofold van Hove singularity and origin of charge order in topological kagome superconductor CsV_3Sb_5 . *Nature Physics* **18**, 301–308 (2022). URL <https://www.nature.com/articles/s41567-021-01451-5>.
- ³³ Ortiz, B. R. *et al.* CsV_3Sb_5 : A Z_2 topological kagome metal with a superconducting ground state. *Phys. Rev. Lett.* **125**, 247002 (2020). URL <https://journals.aps.org/prl/abstract/10.1103/PhysRevLett.125.247002>.
- ³⁴ Yu, F. H. *et al.* Unusual competition of superconductivity and charge-density-wave state in a compressed topological kagome metal. *Nature Communications* **12**, 3645 (2021). URL <https://doi.org/10.1038/s41467-021-23928-w>.
- ³⁵ Du, F. *et al.* Pressure-induced double superconducting domes and charge instability in the kagome

- metal KV_3Sb_5 . *Phys. Rev. B* **103**, L220504 (2021). URL <https://link.aps.org/doi/10.1103/PhysRevB.103.L220504>.
- ³⁶ Oey, Y. M. *et al.* Fermi level tuning and double-dome superconductivity in the kagome metal $\text{CsV}_3\text{Sb}_{5-x}\text{Sn}_x$. *Phys. Rev. Mater.* **6**, L041801 (2022). URL <https://link.aps.org/doi/10.1103/PhysRevMaterials.6.L041801>.
- ³⁷ Li, H. *et al.* Observation of Unconventional Charge Density Wave without Acoustic Phonon Anomaly in Kagome Superconductors AV_3Sb_5 ($A = \text{Rb}, \text{Cs}$). *Phys. Rev. X* **11**, 031050 (2021). URL <https://link.aps.org/doi/10.1103/PhysRevX.11.031050>.
- ³⁸ Wang, Z. *et al.* Electronic nature of chiral charge order in the kagome superconductor CsV_3Sb_5 . *Phys. Rev. B* **104**, 075148 (2021). URL <https://link.aps.org/doi/10.1103/PhysRevB.104.075148>.
- ³⁹ Zhao, H. *et al.* Cascade of correlated electron states in the kagome superconductor CsV_3Sb_5 . *Nature* **599**, 216–221 (2021). URL <https://doi.org/10.1038/s41586-021-03946-w>.
- ⁴⁰ Ortiz, B. R. *et al.* Fermi surface mapping and the nature of charge-density-wave order in the kagome superconductor CsV_3Sb_5 . *Phys. Rev. X* **11**, 041030 (2021). URL <https://link.aps.org/doi/10.1103/PhysRevX.11.041030>.
- ⁴¹ Nie, L. *et al.* Charge-density-wave-driven electronic nematicity in a kagome superconductor. *Nature* **604**, 59–64 (2022). URL <https://doi.org/10.1038/s41586-022-04493-8>.
- ⁴² Zhang, X. *et al.* Destabilization of the charge density wave and the absence of superconductivity in ScV_6Sn_6 under high pressures up to 11 GPa. *Materials* **15** (2022). URL <https://www.mdpi.com/1996-1944/15/20/7372>.
- ⁴³ Yin, J.-X., Lian, B. & Hasan, M. Z. Topological kagome magnets and superconductors. *Nature* **612**, 647–657 (2022). URL <https://doi.org/10.1038/s41586-022-05516-0>.
- ⁴⁴ Sun, Z. *et al.* Observation of topological flat bands in the kagome semiconductor Nb_3Cl_8 . *Nano Letters* **22**, 4596–4602 (2022). URL <https://pubs.acs.org/doi/10.1021/acs.nanolett.2c00778>.
- ⁴⁵ Tanaka, M. *et al.* Topological kagome magnet $\text{Co}_3\text{Sn}_2\text{S}_2$ thin flakes with high electron mobility and large anomalous hall effect. *Nano Letters* **20**, 7476–7481 (2020). URL <https://doi.org/10.1021/acs.nanolett.0c02962>.
- ⁴⁶ Bolens, A. & Nagaosa, N. Topological states on the breathing kagome lattice. *Phys. Rev. B* **99**, 165141 (2019). URL <https://link.aps.org/doi/10.1103/PhysRevB.99.165141>.

- ⁴⁷ Whangbo, M.-H., Canadell, E., Foury, P. & Pouget, J.-P. Hidden fermi surface nesting and charge density wave instability in low-dimensional metals. *Science* **252**, 96–98 (1991). URL <https://www.science.org/doi/abs/10.1126/science.252.5002.96>.
- ⁴⁸ Carpinelli, J. M., Weitering, H. H., Plummer, E. W. & Stumpf, R. Direct observation of a surface charge density wave. *Nature* **381**, 398–400 (1996). URL <https://doi.org/10.1038/381398a0>.
- ⁴⁹ Tam, C. C. *et al.* Charge density waves and fermi surface reconstruction in the clean overdoped cuprate superconductor $Tl_2Ba_2CuO_{6+\delta}$. *Nature Communications* **13**, 570 (2022). URL <https://doi.org/10.1038/s41467-022-28124-y>.
- ⁵⁰ Bosak, A. *et al.* Evidence for nesting-driven charge density wave instabilities in the quasi-two-dimensional material $LaAgSb_2$. *Phys. Rev. Res.* **3**, 033020 (2021). URL <https://link.aps.org/doi/10.1103/PhysRevResearch.3.033020>.
- ⁵¹ Sunko, V. *et al.* Probing spin correlations using angle-resolved photoemission in a coupled metallic/mott insulator system. *Science Advances* **6**, eaaz0611 (2020). URL <https://www.science.org/doi/abs/10.1126/sciadv.aaz0611>.
- ⁵² Li, C. H. *et al.* Electrical detection of charge-current-induced spin polarization due to spin-momentum locking in Bi_2Se_3 . *Nature Nanotechnology* **9**, 218–224 (2014). URL <https://doi.org/10.1038/nnano.2014.16>.
- ⁵³ Li, P. *et al.* Spin-momentum locking and spin-orbit torques in magnetic nano-heterojunctions composed of weyl semimetal WTe_2 . *Nature Communications* **9**, 3990 (2018). URL <https://doi.org/10.1038/s41467-018-06518-1>.
- ⁵⁴ Jiang, Z. *et al.* Enhanced spin seebeck effect signal due to spin-momentum locked topological surface states. *Nature Communications* **7**, 11458 (2016). URL <https://doi.org/10.1038/ncomms11458>.
- ⁵⁵ Luo, S., He, L. & Li, M. Spin-momentum locked interaction between guided photons and surface electrons in topological insulators. *Nature Communications* **8**, 2141 (2017). URL <https://doi.org/10.1038/s41467-017-02264-y>.
- ⁵⁶ Li, Q. *et al.* Bond competition and phase evolution on the $IrTe_2$ surface. *Nature Communications* **5**, 5358 (2014). URL <https://doi.org/10.1038/ncomms6358>.
- ⁵⁷ Fang, A. F., Xu, G., Dong, T., Zheng, P. & Wang, N. L. Structural phase transition in $IrTe_2$: A combined study of optical spectroscopy and band structure calculations. *Scientific Reports* **3**, 1153 (2013). URL <https://doi.org/10.1038/srep01153>.

- ⁵⁸ Tomeljak, A. *et al.* Dynamics of photoinduced charge-density-wave to metal phase transition in $\text{K}_{0.3}\text{MoO}_3$. *Phys. Rev. Lett.* **102**, 066404 (2009). URL <https://link.aps.org/doi/10.1103/PhysRevLett.102.066404>.
- ⁵⁹ Yusupov, R. V., Mertelj, T., Chu, J.-H., Fisher, I. R. & Mihailovic, D. Single-particle and collective mode couplings associated with 1- and 2-directional electronic ordering in metallic RTe_3 (R=Ho, Dy, Tb). *Phys. Rev. Lett.* **101**, 246402 (2008). URL <https://link.aps.org/doi/10.1103/PhysRevLett.101.246402>.
- ⁶⁰ Pokharel, A. R. *et al.* Dynamics of collective modes in an unconventional charge density wave system BaNi_2As_2 . *Communications Physics* **5**, 141 (2022). URL <https://doi.org/10.1038/s42005-022-00919-x>.
- ⁶¹ Möhr-Vorobeva, E. *et al.* Nonthermal melting of a charge density wave in TiSe_2 . *Phys. Rev. Lett.* **107**, 036403 (2011). URL <https://link.aps.org/doi/10.1103/PhysRevLett.107.036403>.
- ⁶² Ravnik, J., Vaskivskyi, I., Mertelj, T. & Mihailovic, D. Real-time observation of the coherent transition to a metastable emergent state in 1T-TaS_2 . *Phys. Rev. B* **97**, 075304 (2018). URL <https://link.aps.org/doi/10.1103/PhysRevB.97.075304>.
- ⁶³ Eichberger, M. *et al.* Snapshots of cooperative atomic motions in the optical suppression of charge density waves. *Nature* **468**, 799–802 (2010). URL <https://doi.org/10.1038/nature09539>.
- ⁶⁴ Tomeljak, A. *et al.* Femtosecond nonequilibrium dynamics in quasi-1d cdw systems $\text{K}_{0.3}\text{MoO}_3$ and $\text{RB}_{0.3}\text{MoO}_3$. *Physica B: Condensed Matter* **404**, 548–551 (2009). URL <https://www.sciencedirect.com/science/article/pii/S092145260800584X>.
- ⁶⁵ Huber, T. *et al.* Coherent structural dynamics of a prototypical charge-density-wave-to-metal transition. *Phys. Rev. Lett.* **113**, 026401 (2014). URL <https://link.aps.org/doi/10.1103/PhysRevLett.113.026401>.
- ⁶⁶ Storeck, G. *et al.* Structural dynamics of incommensurate charge-density waves tracked by ultrafast low-energy electron diffraction. *Structural Dynamics* **7**, 034304 (2020). URL <https://doi.org/10.1063/4.0000018>. <https://doi.org/10.1063/4.0000018>.
- ⁶⁷ Demsar, J., Biljaković, K. & Mihailovic, D. Single particle and collective excitations in the one-dimensional charge density wave solid $\text{K}_{0.3}\text{MoO}_3$ probed in real time by femtosecond spectroscopy. *Phys. Rev. Lett.* **83**, 800–803 (1999). URL <https://link.aps.org/doi/10.1103/PhysRevLett.83.800>.

- ⁶⁸ Chen, R. Y., Zhang, S. J., Zhang, M. Y., Dong, T. & Wang, N. L. Revealing extremely low energy amplitude modes in the charge-density-wave compound LaAgSb₂. *Phys. Rev. Lett.* **118**, 107402 (2017). URL <https://link.aps.org/doi/10.1103/PhysRevLett.118.107402>.
- ⁶⁹ Yusupov, R. *et al.* Coherent dynamics of macroscopic electronic order through a symmetry breaking transition. *Nature Physics* **6**, 681–684 (2010). URL <https://doi.org/10.1038/nphys1738>.
- ⁷⁰ Yoshikawa, N. *et al.* Ultrafast switching to an insulating-like metastable state by amplitudon excitation of a charge density wave. *Nature Physics* **17**, 909–914 (2021). URL <https://doi.org/10.1038/s41567-021-01267-3>.
- ⁷¹ Schaefer, H. *et al.* Dynamics of charge density wave order in the quasi one dimensional conductor (TaSe₄)₂I probed by femtosecond optical spectroscopy. *The European Physical Journal Special Topics* **222**, 1005–1016 (2013). URL <https://doi.org/10.1140/epjst/e2013-01902-4>.
- ⁷² Stojchevska, L. *et al.* Mechanisms of nonthermal destruction of the superconducting state and melting of the charge-density-wave state by femtosecond laser pulses. *Phys. Rev. B* **84**, 180507 (2011). URL <https://link.aps.org/doi/10.1103/PhysRevB.84.180507>.
- ⁷³ Pokharel, G. *et al.* Highly anisotropic magnetism in the vanadium-based kagome metal TbV₆Sn₆. *arXiv:2205.15559* (2022).
- ⁷⁴ Pokharel, G. *et al.* Highly anisotropic magnetism in the vanadium-based kagome metal TbV₆Sn₆. *Phys. Rev. Mater.* **6**, 104202 (2022). URL <https://link.aps.org/doi/10.1103/PhysRevMaterials.6.104202>.
- ⁷⁵ Giannozzi, P. *et al.* Quantum espresso toward the exascale. *The Journal of Chemical Physics* **152**, 154105 (2020). URL <https://doi.org/10.1063/5.0005082>.
- ⁷⁶ Giannozzi, P. *et al.* Quantum espresso: a modular and open-source software project for quantum simulations of materials. *Journal of Physics: Condensed Matter* **21**, 395502 (2009). URL <https://dx.doi.org/10.1088/0953-8984/21/39/395502>.
- ⁷⁷ Giannozzi, P. *et al.* Advanced capabilities for materials modelling with quantum espresso. *Journal of Physics: Condensed Matter* **29**, 465901 (2017). URL <https://dx.doi.org/10.1088/1361-648X/aa8f79>.
- ⁷⁸ Perdew, J. P., Burke, K. & Ernzerhof, M. Generalized gradient approximation made simple. *Phys. Rev. Lett.* **77**, 3865–3868 (1996). URL <https://link.aps.org/doi/10.1103/PhysRevLett.77.3865>.
- ⁷⁹ Hamann, D. R. Optimized norm-conserving vanderbilt pseudopotentials. *Phys. Rev. B* **88**, 085117

(2013). URL <https://link.aps.org/doi/10.1103/PhysRevB.88.085117>.

- ⁸⁰ Wang, V., Xu, N., Liu, J.-C., Tang, G. & Geng, W.-T. Vaspkit: A user-friendly interface facilitating high-throughput computing and analysis using vasp code. *Computer Physics Communications* **267**, 108033 (2021). URL <https://www.sciencedirect.com/science/article/pii/S0010465521001454>.
- ⁸¹ Momma, K. & Izumi, F. VESTA: a three-dimensional visualization system for electronic and structural analysis. *Journal of Applied Crystallography* **41**, 653–658 (2008). URL <https://doi.org/10.1107/S0021889808012016>.
- ⁸² Consiglio, A. *et al.* Van hove tuning of AV_3Sb_5 kagome metals under pressure and strain. *Phys. Rev. B* **105**, 165146 (2022). URL <https://link.aps.org/doi/10.1103/PhysRevB.105.165146>.

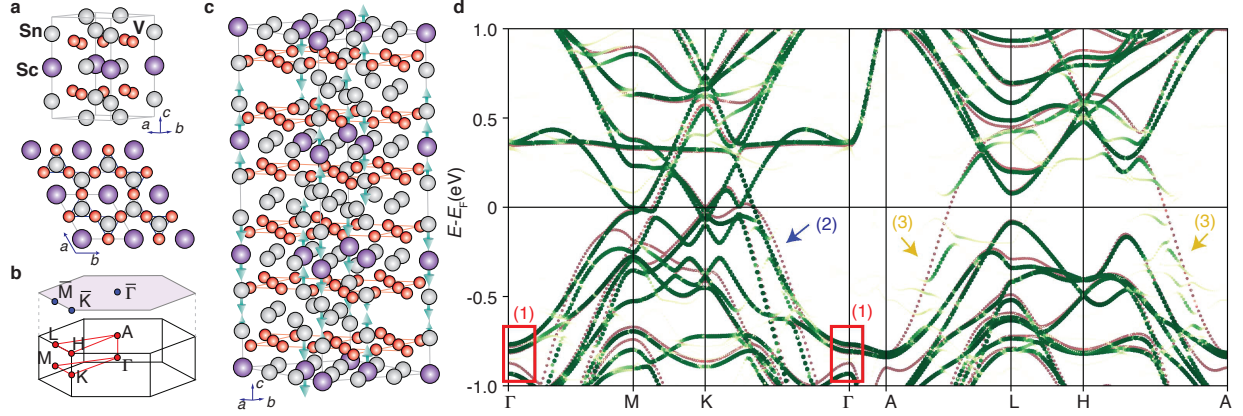


FIG. 1. **Crystal and calculated electronic structure of ScV_6Sn_6 .** **a** Crystal structure without CDW. The top-view corresponds to a 2×2 cell. **b** Brillouin Zone with high-symmetry points and directions. **c** Crystal structure in the CDW phase with the out-of-plane distortions indicated by the arrows. The length of the arrow is proportional to the displacement. **d** Electronic structure of ScV_6Sn_6 without (red lines) and with CDW (green color) along the high symmetry directions. For visual clarity, the pristine bands have been translated in energy by $+0.029$ eV. In this way the van-Hove singularities and the d_{z^2} flat band of the CDW and pristine systems are aligned. It is indeed expected that a structural distortion leads to a tuning in the electronic band structure, especially around E_F ⁸². A similar but disentangled figure can be found in the Supplementary Information. The main changes are here indicated: at Γ (red box, label '1') the CDW induces an increment in the bands separation. Along both Γ -K and Γ -M the bands appear to have slightly different k-loci (blue arrow and label '2'). The main changes are observed along the A-H and A-L directions (yellow arrows and label '3') and are characterized by a marked Sn p_z -states

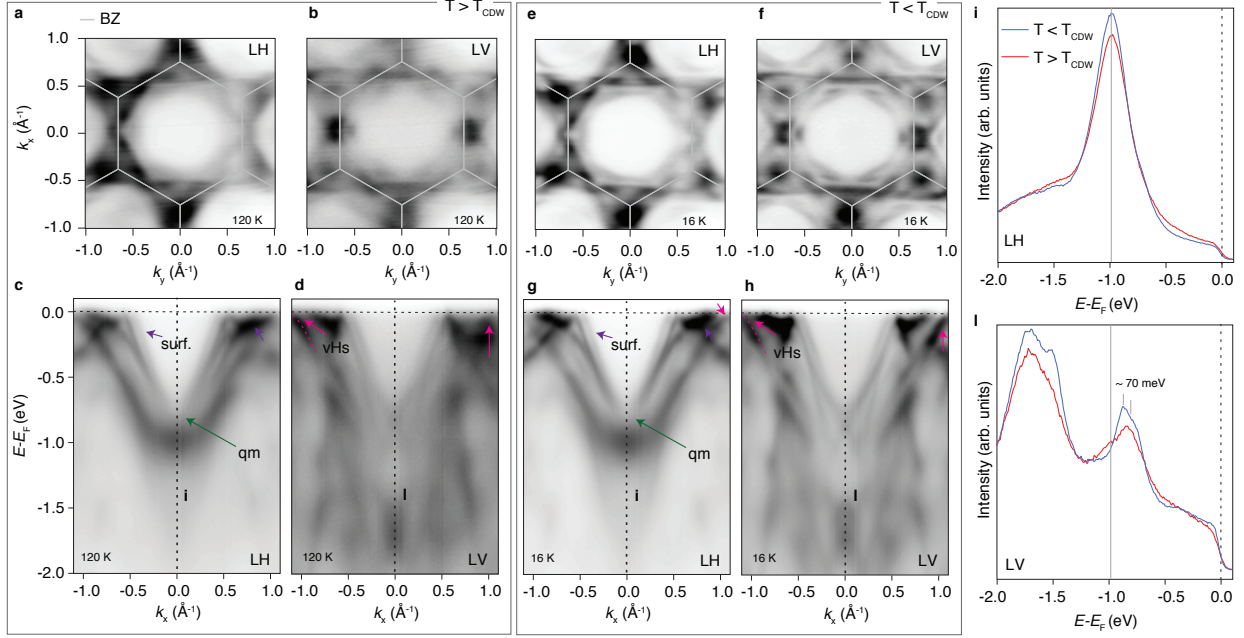


FIG. 2. Measured electronic structure of ScV_6Sn_6 across the CDW critical temperature. Fermi surface of ScV_6Sn_6 collected above T_{CDW} by using linear **a** horizontal and **b** vertical light polarizations and **c-d** corresponding energy versus momentum dispersion along the Γ -K-M direction of the Brillouin zone. Fermi surface of ScV_6Sn_6 collected below T_{CDW} by using linear **e** horizontal and **f** vertical light polarizations and **g-h** corresponding energy versus momentum dispersion along the Γ -K-M direction of the Brillouin zone. **i-l** Energy distribution curve (EDC) extracted at the Γ -point for LH and **l** LV polarization, across the transition temperature. LV reveals more spectral details, including a small doublet.

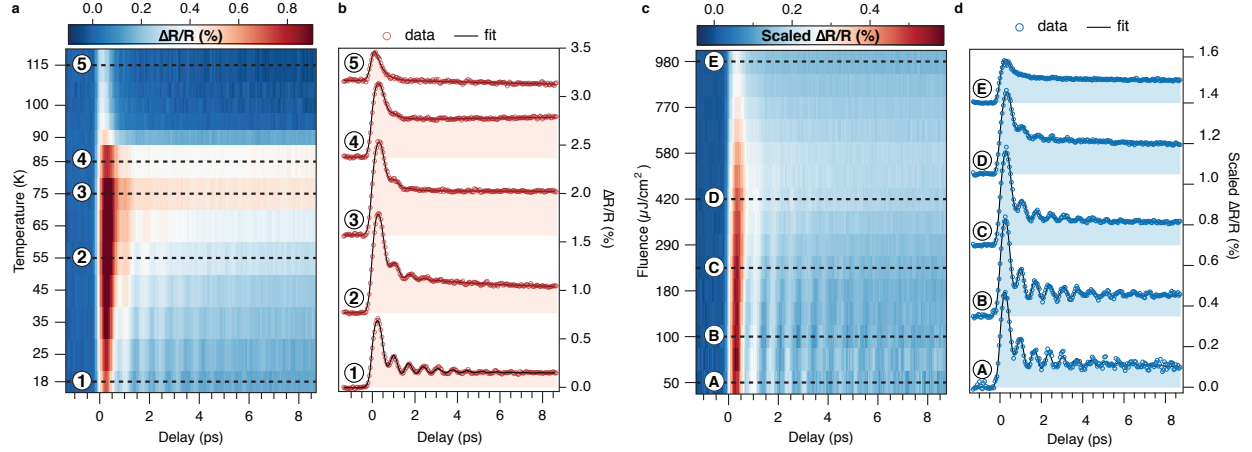


FIG. 3. Temperature and fluence dependent-dynamics of ScV_6Sn_6 . **a** Evolution of $\Delta R/R$ as a function of the temperature in the temperature range across T_{CDW} , showing the signatures of the phase transition around 90 K. In the low temperature CDW phase a clear oscillatory response is observed. **b** $\Delta R/R$ profiles extracted from **a** at selected temperatures, showing the evolution of the dynamics across the phase transition. **c** Evolution of the scaled $\Delta R/R$ as a function of the fluence across T_{CDW} . The traces are scaled to the fluence to ease the visualization upon approaching the photoinduced phase transition. **d** Scaled $\Delta R/R$ profiles extracted from **c** at selected fluences.

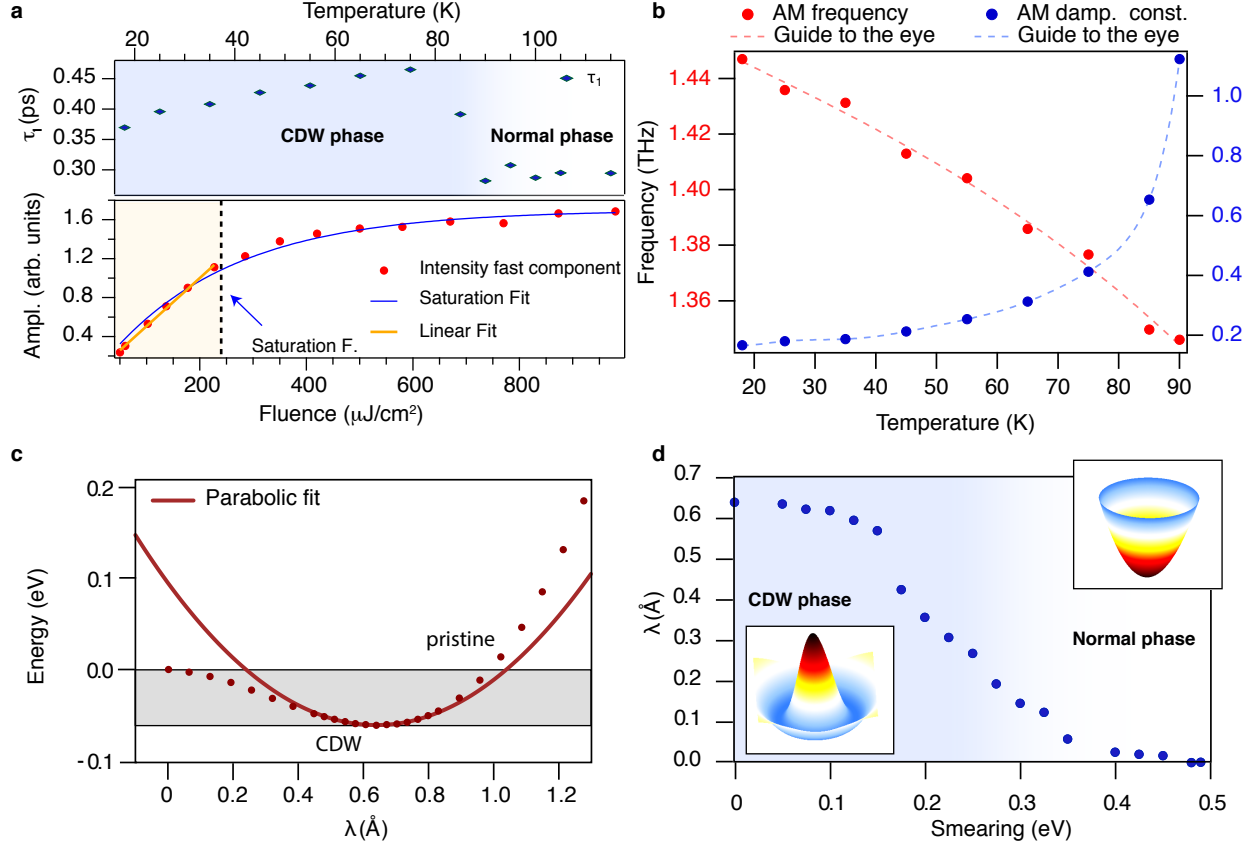


FIG. 4. Evolution of significant fit parameters. **a** Evolution of the lifetime of the first fast decay (τ_1) as a function of the temperature (top panel) and evolution of the amplitude of the fast peak as function of fluence (bottom panel). **b** Evolution of the frequency and the damping constant of the amplitude mode as a function of the temperature. **c** Total energy of the ScV_6Sn_6 constant-volume superlattice while interpolating between the pristine, the CDW and the exaggerated CDW phases. $\lambda = 0.00 \text{ \AA}$ means that the displacement vector has a vanishing norm, i.e. we are in the reference starting point (the pristine phase). When $\lambda = 0.64 \text{ \AA}$, the norm of the displacement vector is $\|\vec{e}\| = \lambda$, hence we are in the CDW phase. When further increasing the norm of the displacement vector, we are describing an exaggerated CDW phase. The parabola represented by a continuous line is the quadratic fit of the energy profile, around the minimum. The quadratic coefficient is related to the spring constant k and frequency ω of the CDW amplitude mode (more details in the Methods section). **d** Norm of the 351-dimensional displacement vector \vec{e} among the CDW and pristine structures, as a function of the electronic (gaussian) smearing σ used during the constant-volume ionic relaxation.

I. SUPPLEMENTARY INFORMATION

II. ARPES AND MEASUREMENTS WITHOUT SURFACE STATES

The ARPES measurements have been performed across the transition temperature, i.e. 98 K, for ScV_6Sn_6 both with and without the presence of surface states. While the presence of surface states is guaranteed by a successful UHV cleave, in order to suppress them and to remain on the same sample's spot precautions are needed. Indeed, we noticed that by cleaving the samples both at 16 K and at 120 K (in the CDW phase and above it) the surface states are present. However, if one cleaves the samples at 16 K (or at 120 K) and varies the temperature up to 120 K (or down to 16 K) the surface states are killed, possibly by absorption onto the sample's surface following a temperature change. To suppress the surface states an overall reduction of the ARPES data quality was observed. In order to get high quality surface states, as in the main text, we cleaved the same sample one time at 16 K and one time at 120 K. Then, in order to detect the bulk electronic structure as in S1, we waited a sufficient time at the selected temperature until the surface states were suppressed by aging. This ensures a better overall quality of the ARPES data, compared to a forced aging by thermal process, and allows us to be sure to be on the same area of the sample with the light beam. We noticed also a variation in the aging time. For samples cleaved at 120 K, despite the initial lower quality, the surface states resisted for a longer time, i.e. 15-24 hours. For samples cleaved at 16 K, we noticed an initial better quality for the ARPES data, but a faster degradation time of about 4-6 hours. For the data in the main text, above the transition temperature, the surface states appear weaker. Such a weaker intensity recorded for the surface states above T_{CDW} is not surprising given the more pronounced degradation expected for the highest temperature cleave. In this regard, we even noticed that by increasing slightly further the temperature, the surface states get completely suppressed. However, the electronic structure remains the same, with no changes in van-Hove singularities (red arrows in Fig.2 of the main text) and overall dispersion.

III. ARPES AND MEASUREMENTS ALONG A-H AND A-L DIRECTIONS

As we showed in the main text, the DFT calculations capture very well the effects of the CDW on the electronic structure of ScV_6Sn_6 . Along the high-symmetry directions Γ -M-K, we have the most favorable matrix elements and the strongest spectroscopic signal. In these conditions, the main changes are visible at the Γ point as an increase in the energy separation of some states

locates around -0.8 eV. Nevertheless, the DFT predicts the largest changes to occur in the k_x - k_y plane located between two consecutive Γ -points. Here we used 65 eV photon energy (with both linear vertical and horizontal light polarizations) to capture such a plane and also the A-H and A-L directions, as shown in the Brillouin zone of Fig.1 of the main text. To note that despite the CDW-induced changes are supposed to be prominent here, the photoemission matrix elements reduces significantly the intensity of the electronic structure and, together with a rather significant k_z broadening, the CDW changes are not easily detected. This is further challenged by the fact that in the low temperature phase, the spectral weight rapidly diminishes away from the gaps and still, the main intensity 'follow' the dispersion of the bands above T_{CDW} , as visible in the DFT of the main text. However, we will here show the results in these conditions.

First of all, we show the Fermi surface maps of the systems within the k_x - k_y plane centred in the A point, along with the dispersion along the L-A-H-L, in figure 3 and 4, respectively. One can notice that apart from the better intensity and resolution gained in the low temperature phase and due to sharper features, overall there are no significant changes observed or at least, the changes are not big enough to justify them as effect of the CDW. To better see possible changes, we also report the very-high-resolution ARPES data along the A-H-L direction. Still, the data corroborate our previous conclusions.

IV. TR-OS ANALYSIS AND DETAILS

In order to describe the incoherent part of the $\Delta R/R$ signal, we used a double-exponential function, $\Delta R/R \propto A_1 e^{-t/\tau_1} + A_2 e^{-t/\tau_2} + bkg$, where $A_1 e^{-t/\tau_1}$ describes the fast decay process (first stage of the CDW) while $A_2 e^{-t/\tau_2}$ describes the slower recovery process (second stage of the CDW). The bkg term is used to take into account an extremely slow recovery process that can be described by a constant value in our time window.

In order to quantitatively analyze the oscillatory component of the $\Delta R/R$ signal, we considered the Fourier transform of the residuals obtained by considering the difference between the data and the double-exponential fit function described above. The complete fit function, resulting in the black lines of Fig.3 of the main text, has been obtained by adding a damped cosine oscillation,

$$A_p e^{-t/\tau_p} \cos(w_p t + \phi_p).$$

To give a rough estimate the induced heating by the pump, we assumed, reasonably, that the heat capacity of ScV_6Sn_6 is of the same order of magnitude of the ones reported for similar kagome systems (both binary and ternary). We do not expect that the temperature deviates more than 20 K upon pump application.

V. ELECTRONIC AND PHONONIC BAND STRUCTURES DETAILS

In this section are reported complementary figures, supporting the statements and the results of the main text. In particular, we report the calculated electronic structure with and without CDW separately (Fig. 8), and the phonon density of states and the mechanism by which the phonon frequency has been estimated (Fig. 9). In addition (Fig. 10), we also show the data from time-resolved optical spectroscopy documenting the evolution of the fast component. Such evolution is reminiscent of the one observed in time-resolved photoelectron spectroscopy, and associated to the electronic degrees of freedom.

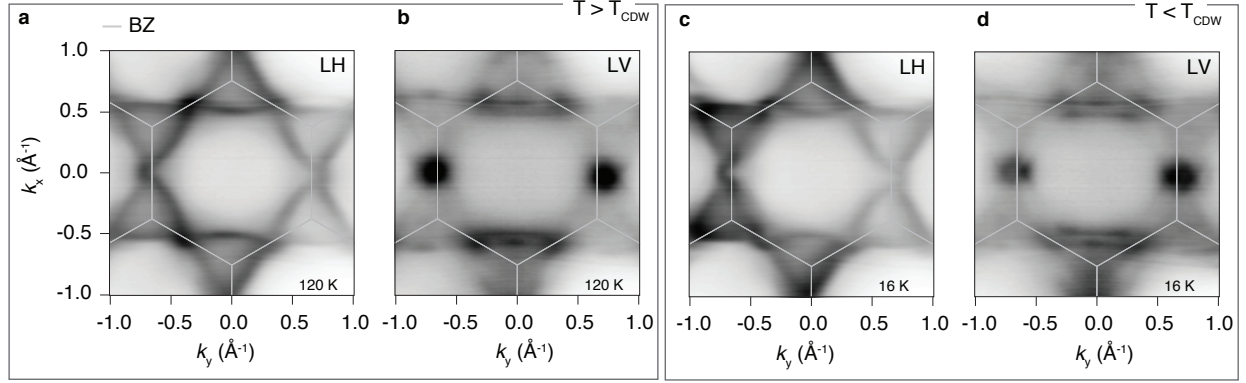


FIG. 5. Fermi surfaces of ScV_6Sn_6 kagome metal without surface states. **a** Linear horizontal and **b** linear vertical polarization Fermi surface maps collected for ScV_6Sn_6 above the transition temperature. **c** Linear horizontal and **d** linear vertical polarization Fermi surface maps collected for ScV_6Sn_6 below the transition temperature. In order to be sure about the absence of surface states, the samples were left for a significant time in the same positions and same conditions (approximately 24 h) and they showed a natural aging effect, which resulted in the removal of the surface states manifold.

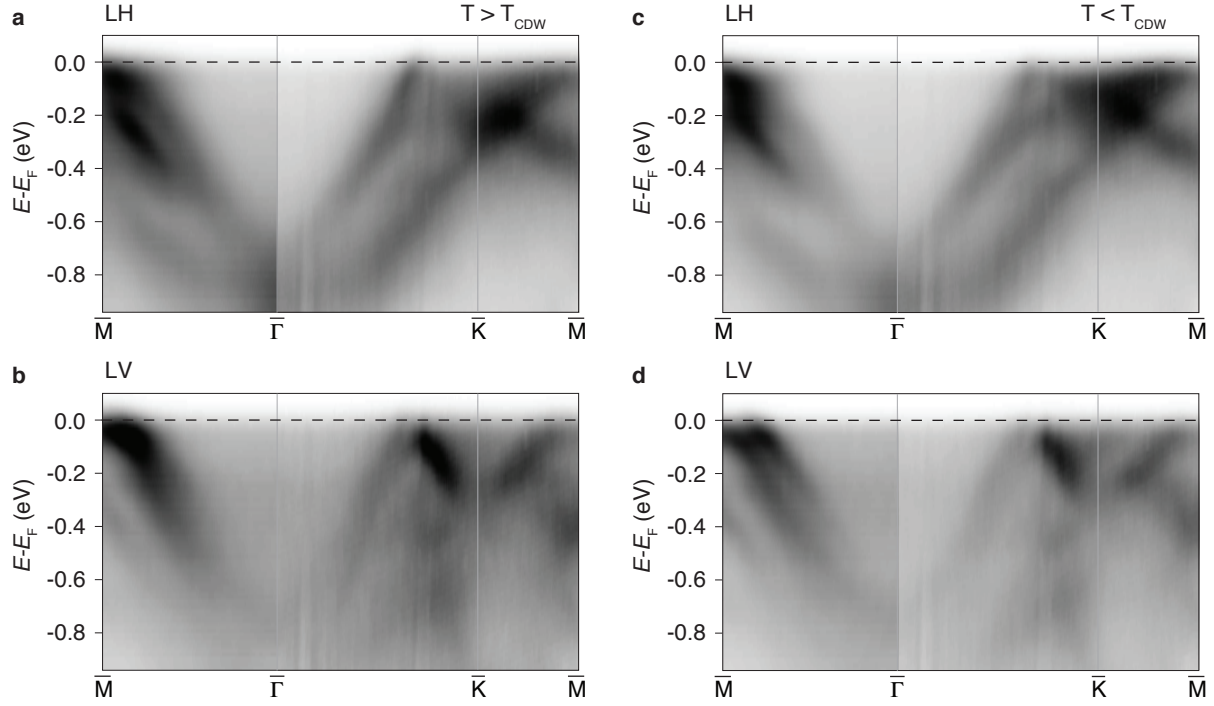


FIG. 6. **Energy vs momentum dispersion of ScV_6Sn_6 kagome metal without surface states.** **a** linear horizontal and **b** vertical polarization spectra along the Γ -K-M direction of the BZ obtained for ScV_6Sn_6 after the surface states were suppressed as in S1, above T_{CDW} . **c** linear horizontal and **d** vertical polarization spectra along the Γ -K-M direction of the BZ obtained for ScV_6Sn_6 after the surface states were suppressed as in S1, below T_{CDW} .

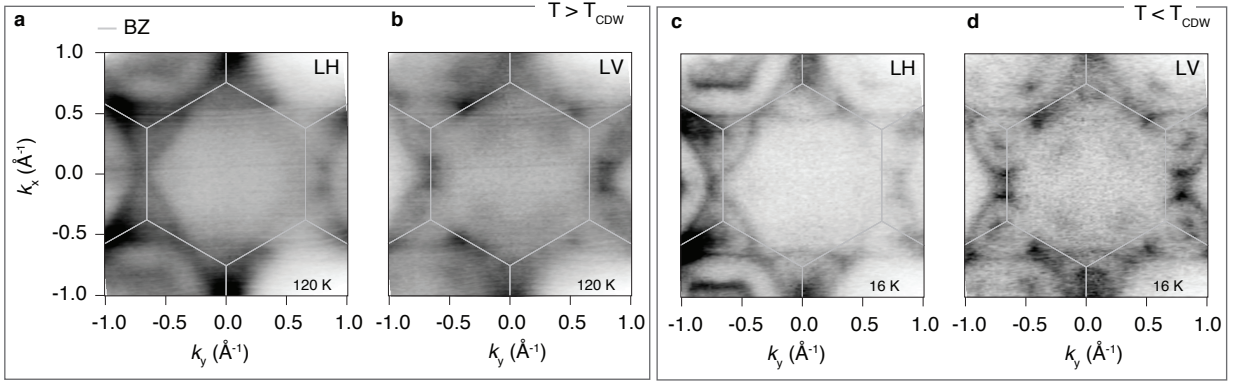


FIG. 7. **Fermi surfaces of ScV_6Sn_6 kagome metal centred in the plane of the A point, i.e. 65 eV.** **a** Linear horizontal and **b** linear vertical polarization Fermi surface maps collected for ScV_6Sn_6 above the transition temperature. **c** Linear horizontal and **d** linear vertical polarization Fermi surface maps collected for ScV_6Sn_6 below the transition temperature. As one can see, the low temperature data appear sharper due to the reduced thermal broadening.

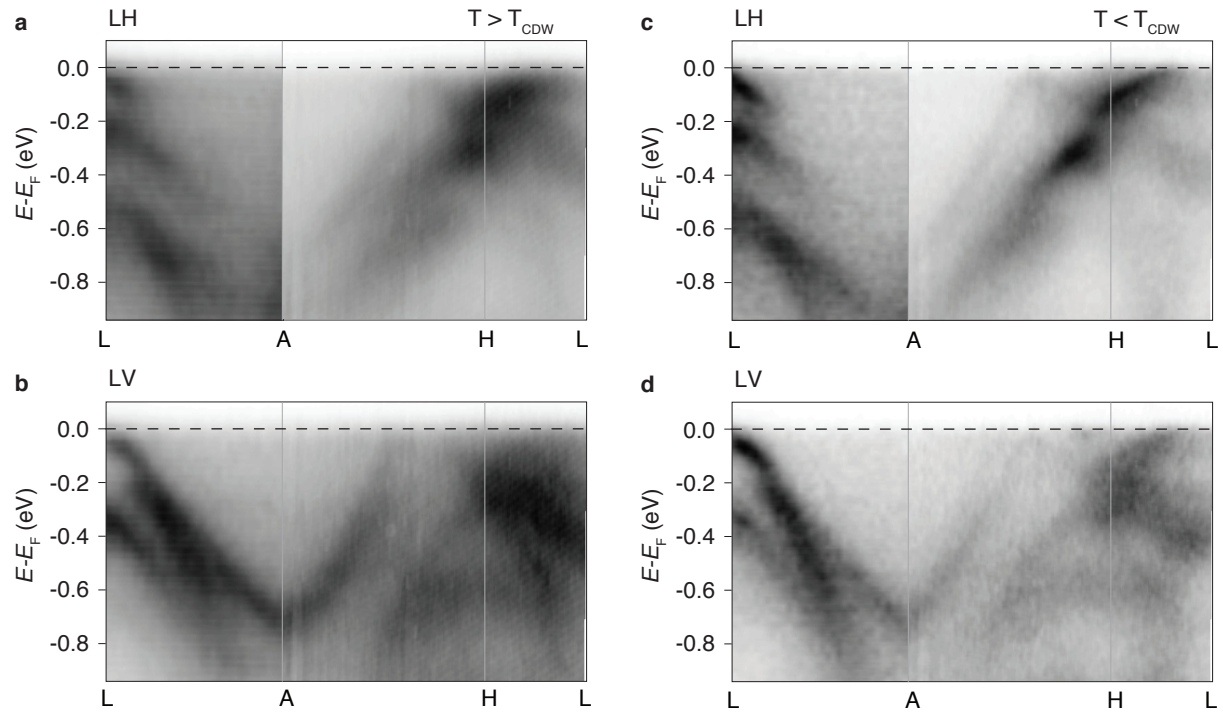


FIG. 8. **Energy vs momentum dispersion of ScV_6Sn_6 kagome metal centred in the plane of the A point, i.e. 65 eV.** **a** linear horizontal and **b** vertical polarization spectra along the L-A-H-L direction of the BZ obtained for ScV_6Sn_6 , above T_{CDW} . **c** linear horizontal and **d** vertical polarization spectra along the L-A-H-L direction of the BZ obtained for ScV_6Sn_6 , below T_{CDW} .

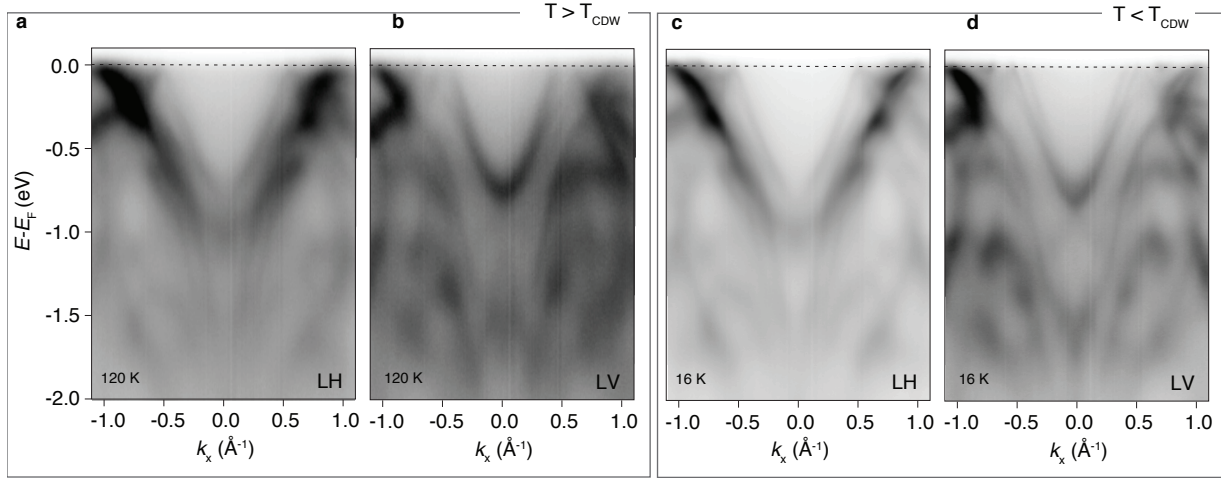


FIG. 9. **High-resolution Energy vs momentum dispersion of ScV_6Sn_6 kagome metal along the A-H-L directions** **a** linear horizontal and **b** vertical polarization spectra along the A-H-L direction of the BZ obtained for ScV_6Sn_6 , above T_{CDW} . **c** linear horizontal and **d** vertical polarization spectra along the A-H-L direction of the BZ obtained for ScV_6Sn_6 , below T_{CDW} .

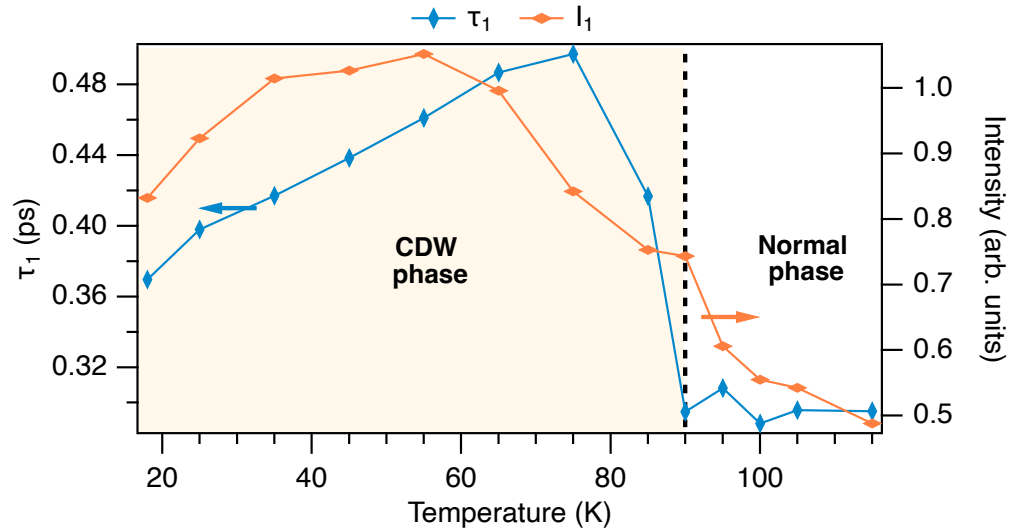


FIG. 10. **Fast decay evolution as function of temperature.** Evolution of the lifetime (τ_1 , left axis) and of the amplitude (I_1 , right axis) of the first fast decay as a function of the temperature. As one can see, contrary to the amplitude decay as function of fluence (Fig. 4 of the main text), which shows a saturation, here, I_1 has a very similar behaviour to the lifetime as function of temperature.

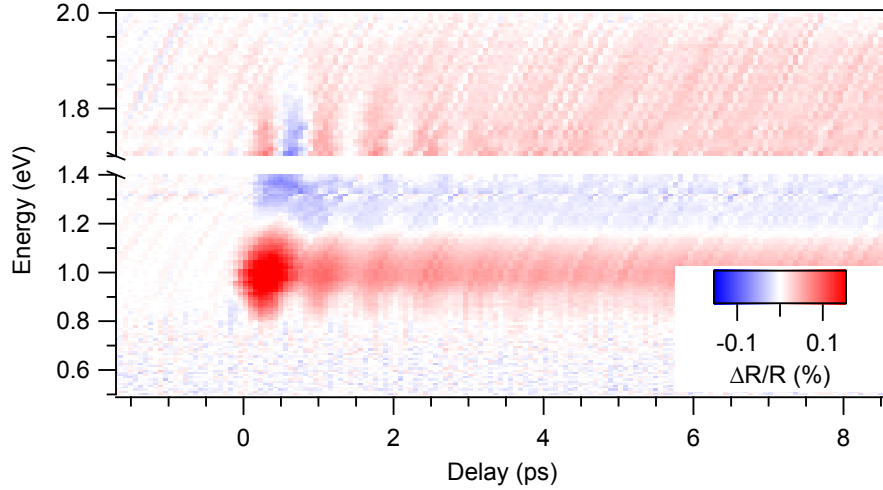


FIG. 11. **Time- and frequency- resolved reflectivity.** The reflectivity is reported as energy versus time for samples kept at 30 K.

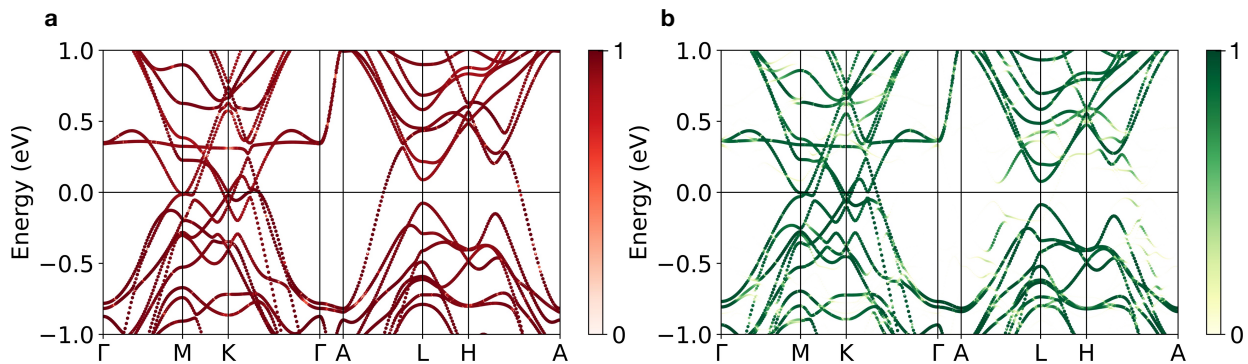


FIG. 12. **Band structure unfolding of the pristine phase vs the CDW one** **a** Electronic band structure of the pristine phase, with color-bar on the right side. The plot has been obtained unfolding the same superlattice of the CDW phase, without the lattice distortion. The bands have been shifted upward by 0.029 eV. **b** Electronic band structure of the CDW phase, with color-bar on the right side. Note how, in this case, a wider range of colors needs to be employed.

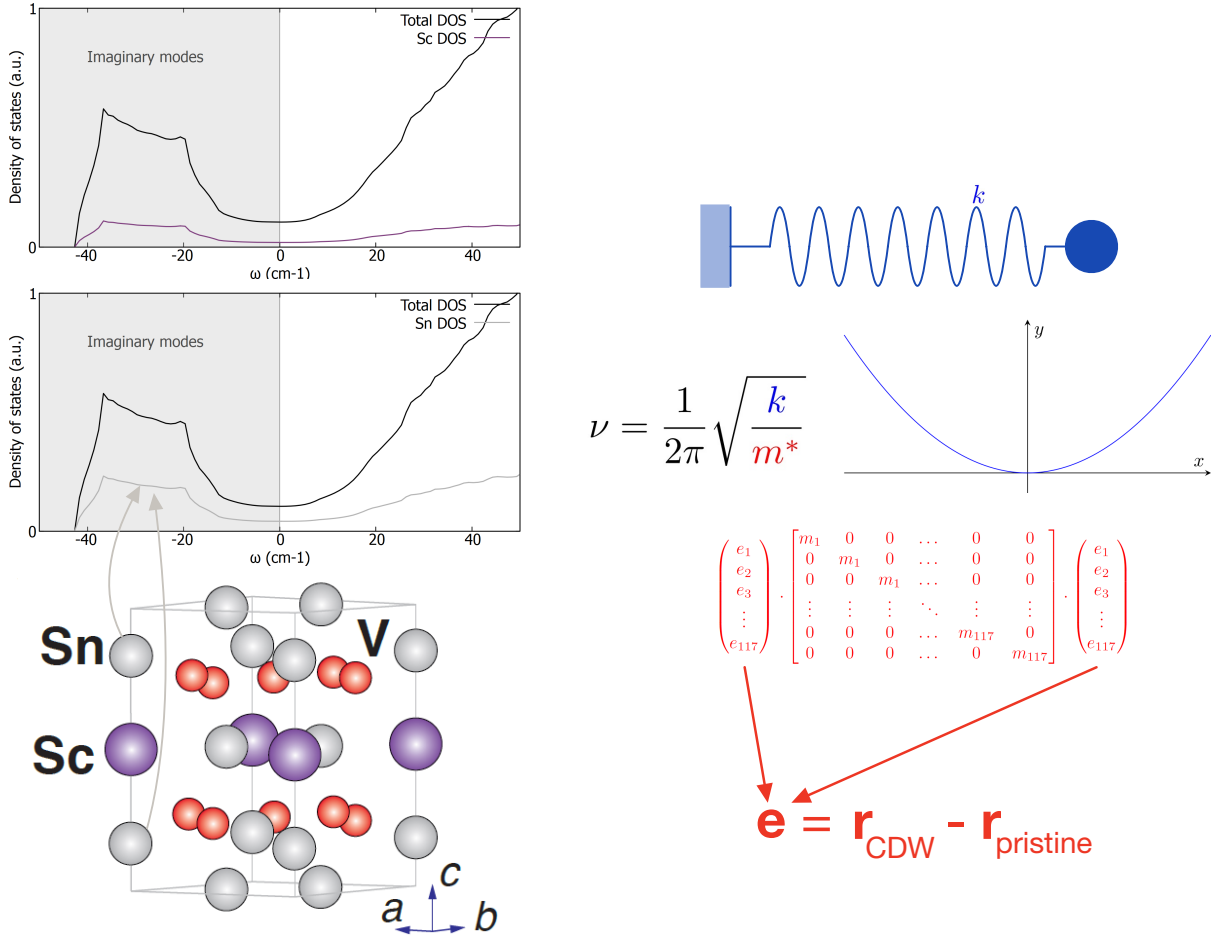


FIG. 13. **Phonon and CDW theoretical details** **a** Density of states of phonons in ScV6Sn6. The imaginary modes, indicating a dynamical instability, are only due to the Sc atom, and the Sn atoms with the same scandium's (x, y) coordinates. Note that some atoms in the cell are represented more than once, because of the periodic boundary conditions. **b** Schematic sketch of the procedure followed to compute the frequency of the phonon mode ($\nu = 1.42$ THz). Red colors refer to the effective mass m^* , obtained from the mass tensor and the (normalized) displacement vector. Blue color refers to the spring constant, obtained by doubling the quadratic coefficient of the parabola. This parabola has been obtained via a quadratic fit, about one of the two minima of the double-well potential energy profile.

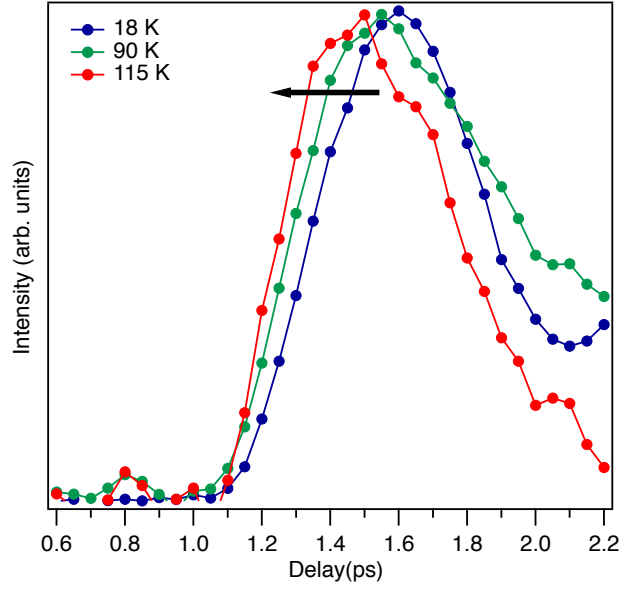


FIG. 14. **Evolution of the rising edge as function of time and temperature.** Evolution of the rising edge of the $\Delta R/R$ signal at the arrival of the pump pulse, for three selected temperatures (below T_{CDW} , at T_{CDW} and above T_{CDW}). Above the critical temperature the maximum of the $\Delta R/R$ signal is reached 150 fs faster than in the CDW phase. The three traces have been normalized at their maximum intensity.